International Journal of Heat and Mass Transfer 51 (2008) 6243–6253

Contents lists available at ScienceDirect

International Journal of Heat and Mass Transfer

journal homepage: www.elsevier.com/locate/ijhmt

Effects of hole spacing on spatially-resolved jet array impingement heat transfer

Matt Goodro[a], Jongmyung Park[b], Phil Ligrani[a,*], Mike Fox[c,1], Hee-Koo Moon[c,1]

[a] Department of Engineering Science, University of Oxford, Parks Road, Oxford OX1 3PJ, UK
[b] KIGAM (Korea Insititue of Geoscience and Mineral Resources), 30 Gajeong-dong, Yuseong-gu, Daejeon 305-350, Korea
[c] Aero/Thermal and Heat Transfer, Solar Turbines Inc., 2200 Pacific Highway, P.O. Box 85376, Mail Zone C-9 San Diego, CA 92186-5376, USA

ARTICLE INFO

Article history:
Received 21 March 2007
Available online 7 July 2008

ABSTRACT

Data which illustrate the effects of hole spacing on spatially-resolved heat transfer from an array of jets impinging on a flat plate are presented. Considered are Reynolds numbers ranging from 8200 to 30,500, and Mach numbers from 0.1 to 0.6. The spacing of the holes used to produce the impinging jets is either 8*D* or 12*D* in both the streamwise and spanwise directions. Local and spatially-averaged Nusselt numbers show strong dependence on the impingement jet Reynolds number for both situations, with negligible variations between $Ma = 0.1$ and 0.2 at constant Reynolds number. Experimental data, taken at Mach numbers greater than 0.2, while maintaining constant Reynolds number, show that Mach number has a significant impact on overall heat transfer. For 8*D* spacing, heat transfer is augmented significantly as the Mach number increases, and for hole spacing of 12*D*, heat transfer also increases significantly as the Mach number increases. Also included is a new correlation, based on that of Florschuetz et al. [L.W. Florschuetz, C.R. Truman, D.E. Metzger, Streamwise flow and heat transfer distributions for jet array impingement with crossflow, ASME Trans.–J. Heat Transfer 103 (1981) 337–342], as an impingement design tool.

© 2008 Elsevier Ltd. All rights reserved.

1. Introduction

Undesired heat loads are often created by exposure to hot gases or liquids. Impingement cooling is widely used to remove such loads. It is an attractive method of heat management because its effectiveness is relatively high, making it a viable tool for heat load management. The main objective of such cooling is maximum heat removal with minimal coolant mass flow rates. As a result, impinging jets are often delivered by orifices which have been cast or machined into internal structural members contained within components which are part of the particular application. For example, when utilized to cool leading edge regions of turbine blades and vanes, the impingement air enters the leading edge cavity from an adjacent cavity through a series of crossover holes on the partition wall between the two cavities. The crossover jets then impinge on the concave leading-edge wall and then exit either through film cooling holes, or though exit passages which lead to another part of the airfoil. With this arrangement, spanwise lines of impingement jets are produced, which direct cooling air on high external heat load regions, such as the stagnation region [1]. Impingement cooling is also often used to cool parts of the combustor in gas turbine engines, including combustion chamber liners, transition pieces, and splash plates. In each case, impinging jets are used individually or in arrays [2].

Impingement cooling has experienced extensive use in industrial applications. As such, extensive literature on impingement cooling is available. Most existing investigations consider the effects of changing impingement plate geometric and configuration parameters, and physical parameters in flows with low Mach numbers, and relatively low speeds. Of these studies, Kercher and Tabakoff [3] present spatially-averaged surface heat transfer coefficients beneath an array of impinging jets in low-speed flow for Reynolds numbers from 3×10^2 to 3×10^4, X/D and Y/D from 3.1 to 12.5, and Z/D from 1.0 to 4.8. Spent air flow from the impingement array exits the flow passage in one direction. Inline array of holes is employed. According to these investigators, the spatially-averaged heat transfer coefficients are dominated by the Reynolds number, and streamwise/spanwise hole spacing. Of studies which consider heat transfer within airfoil leading edge regions, Metzger et al. [4] and Chupp et al. [5] address heat transfer with a semi-circular concave region with a line of circular jets impinging on the apex. The effects of target spacing, hole spacing, and jet Reynolds number are considered. Metzger and Korstad [6] examine the influences of cross-flow on a single line of jets, emerging from circular holes, placed on one wall of a channel. They show that target spacing, jet Reynolds number, and the relative strengths of the jet flow and the cross flow influence heat transfer on the target wall.

Like the investigation of Kercher and Tabakoff [3], Chance [7] also investigates low-speed impingement cooling with spent air constrained to flow out only one side of the flow passage. He describes static pressure variations with the impingement passage which become larger with higher cross-flow velocities as Z/d

---

[*] Corresponding author. Tel.: +44 (0) 1865 288734; fax: +44 (0) 1865 288756.
E-mail address: p_ligrani@msn.com (P. Ligrani).
[1] Tel.: +1 (619) 544 5477; pager: +1 (619) 526 4601.

0017-9310/$ - see front matter © 2008 Elsevier Ltd. All rights reserved.
doi:10.1016/j.ijheatmasstransfer.2008.05.004

Nomenclature

A	impingement hole area
A_{ht}	heat transfer area on the target plate
c_{a}	impingement air flow sonic velocity
C_{D}	discharge coefficient
D	diameter of an individual impingement hole
G_{c}	crossflow mass velocity
G_{j}	jet mass velocity
h_{loss}	heat transfer coefficient to account for convection and radiation loss from back side of target plate
k	ratio of specific heats
$\dot{m}$	impingement air mass flow rate
Ma	impingement air flow Mach number
Mi	impingement air flow ideal Mach number
Nu	local Nusselt number
$\underline{\overline{Nu}}$	line-averaged Nusselt number
$\overline{\overline{Nu}}$	spatially-averaged Nusselt number
P_{a}	impingement air static pressure
P_{oj}	impingement air stagnation pressure
Q	total power provided to the thermofoil heater
q_{rf}	radiation heat flux from front side (or impingement side) of the target plate
q_{rb}	radiation heat flux from back side of the target plate
q_{cf}	convection heat flux from front side (or impingement side) of the target plate
q_{cb}	convection heat flux from back side of the target plate
R	ideal gas constant
Re_j	impingement air flow Reynolds number
T_{ambient}	ambient static temperature
T_{b}	local temperature on the back surface of the polystyrene target plate
T_{W}	local target surface temperature on the surface of the heater adjacent impingement air
T_{i}	impingement air ideal static temperature
T_j	impingement air static temperature
T_{oj}	impingement air stagnation temperature
T_{tc}	local thermocouple temperature between the heater and the polystyrene target plate
u_{a}	impingement air velocity
$u_{\mathrm{crossflow}}$	crossflow air velocity
u_{i}	impingement air ideal velocity
u_{jet}	jet air velocity
x	streamwise coordinate
y	spanwise coordinate
z	normal coordinate
X	streamwise distance between centerlines of adjacent impingement holes
Y	spanwise distance between centerlines of adjacent impingement holes
Z	distance between target plate and impingement hole plate

Greek symbols

α	air thermal conductivity
ρ_{a}	impingement air static density
ρ_{i}	impingement air ideal static density
μ	absolute viscosity
σ	Boltzman constant,
ε_{f}	emissivity of the front surface of the target plate
$\varepsilon_{\mathrm{inf}}$	emissivity of a plate located opposite to the target plate

decreases. Also addressed in this investigation are data at Reynolds numbers from 6×10^3 to 5×10^4, square, equilateral triangle, and rectangular jet arrays, Z/d values of 2, 3, 4, 6, and 8, and ratios of impingement to surface absolute temperature of 0.77, 1.27, and 1.54. In another paper, Metzger et al. [8] indicate that in-line jet impingement hole patterns provide better heat transfer than staggered arrangements. Investigated are Z/D values of 1, 2, and 3, X/D and Y/D ranging from 6 to 32, and Reynolds numbers from 5×10^3 to 2×10^4. Florschuetz et al. [9] describe a continuation of this investigation, wherein Reynolds numbers from 2.5×10^3 to 7×10^4, inline and staggered hole patterns, Z/D from 1 to 3, X/D from 5 to 15, and Y/D from 4 to 8 are considered. In this investigation, the temperature difference between the impingement surface temperature and the plenum air temperature is normally 15–30 K. As for the previous investigation, impinging air is again constrained to exit in a single direction from the channel formed between the impingement plate and the target plate. Included are data on channel cross flow mass velocity and jet mass velocity (where ratios range from 0 to 0.8), as well as a correlation with gives Nusselt number dependence on these parameters, as well as on jet impingement plate geometry, Prandtl number, and Reynolds number.

Obot and Trabold [10] consider different cross-flow schemes on impingement heat transfer in low-speed flows. Impingement jet Reynolds numbers from 1×10^3 to 2.1×10^4, Z/D values from 2 to 16, X/D values of 5 and 10, and Y/D values of 4 and 8 are employed. According to these investigators, for a given crossflow scheme and constant jet diameter D, higher heat transfer coefficients are obtained as the number of jets over a fixed target area increases. Bunker and Metzger [11] present detailed local heat transfer distributions due to line jet impingement for leading edge regions, both with and without film extraction effects. Fox et al. [12] examine the effects of unsteady vortical structures on the adiabatic wall temperature distribution produced by a single impinging jet. Secondary vortex structures within the jet are described which alter adiabatic surface temperatures when the target plate is near the jet nozzle (i.e. Z/D of 1, 2, or 4). Bailey and Bunker [13] investigate impingement arrays with inline jets in a “square array”, with axial and lateral jet spacings of 3, 6, and 9. Reynolds numbers range from 1.4×10^4 to 6.5×10^4, Mach numbers are relatively low, and jet plate-to-target spacings range from 1.25 to 5.5 impingement hole diameters. Included are correlations developed from these data which extend the range of applicability of the correlations presented by Florschuetz et al. [9]. They also show that, for sparse impingement arrays, each jet behaves independently.

Other recent studies consider the effects of jet impingement on a leading edge/concave wall with roughness [14], and the effects of jets with mist and steam on a concave target surface [15]. Parsons et al. [16,17], Parsons and Han [18], Epstein et al. [19], and Mattern and Hennecke [20] show that rotational effects are important for jets impinging on flat surfaces at relatively low Reynolds numbers. In another recent investigation which employs flat target plates, Brevet et al. [21] consider one row of impinging jets in a test section with low speed flow in which the spent air is again constrained to exit in one direction. Effects of impingement distance, Reynolds number, and spanwise hole spacing on Nusselt number distributions lead to recommendations for optimal Z/D values of 2–5, and optimal spanwise hole spacings of 4–5 hole diameters. Data obtained at Reynolds numbers from 5×10^3 to 2×10^4, Z/D of 1, 2, 5, and 10, and X/D, Y/D values of 2, 4, 6, and 10 also show that local and spatially-averaged Nusselt numbers increase substantially with Reynolds number. Brevet et al. [22] describe recovery factors and Nusselt numbers measured on a flat target surface beneath a single, compressible impingement jet. Results are given for Z/D ratios from 2 to 10, at different Mach numbers from 0.02 to 0.69. Data sets with different Mach numbers and constant Reynolds number are obtained using different impingement hole plates with different hole diameters from 3 to 15 mm.

Behahani et al. [23] present correlation equations for local heat transfer due to staggered arrays of impinging circular air jets. Two different jet-to-jet spacings, $4D$ and $8D$, and three different Reynolds numbers, 5000, 10,000, and 15,000, are employed. The investigations show that area-averaged Nusselt numbers become smaller because the cooling area is smaller, when the jet-to-jet spacing is larger. San and Lai [24] investigate jet-to-jet spacing to optimize surface heat transfer for staggered arrays of impinging air jets. Five jets, two exit sides, and Reynolds numbers between 10,000 and 30,000 are employed. For Reynolds numbers of 10,000–30,000, they recommend optimal jet-to-jet spacings of $8D$, $12D$, and $6D$ for jet hole exit to target plate distances of $2D$, $3D$, and $5D$, respectively. Downs and James [25], Jambunathan et al. [26], and Viskanta [27] present reviews of several other jet impingement investigations.

The present study is aimed at providing *new spatially-resolved impingement heat transfer data* on the effects of hole spacing at different Reynolds number and Mach numbers. Hole spacings of $8D$ and $12D$ are employed. The thickness of each impingement plate is $1D$, and the spacing between the hole exit planes and the target plate is $3D$. Included are discharge coefficients, crossflow-to-jet mass velocity ratios, as well as local, line-averaged and spatially-averaged Nusselt numbers. The present study examines impingement array behavior for Reynolds numbers of 8200, 17,300, and 30,000 and Mach numbers from 0.1 to 0.6. The results from the present investigation are unique and different from data given in other recent studies because the flow conditions and configurations employed are *new*. As such, the data obtained are important because they illustrate the dependence of local and spatially-averaged Nusselt numbers on jet Mach number and jet Reynolds number, for different hole jet spacings. This is significant because the different hole spacings result in different interactions between adjacent jets and between jets and wall boundary layers, which, when coupled with compressibility, can give important local Nusselt number dependence on Mach number.

2. Experimental apparatus and procedures

2.1. Impingement flow facility, and impingement plate

Schematic diagrams of the facility used for heat transfer measurements are presented in Figs. 1 and 2. The facility is constructed of 6.1 mm thick ASTM A38 steel plates, and A53 Grade B ARW steel piping. The air stream circulates in a closed loop to facilitate impingement air cooling. To achieve the Reynolds number of the present study, a New York Blower Co. 7.5 HP, size 1808 pressure blower is employed. The air mass flow rate provided to the test section is measured using an ASME standard orifice plate, flow-mounted calibrated copper–constantan thermocouples, and Validyne DP15 pressure transducers (with diaphragms rated at 13.8 or 34.5 kPa) connected to DP10D Carrier Demodulators. The blower exits into a series of two plenums arranged in series, where the upstream plenum is .63 m in length along each side, and the downstream plenum dimensions are .63 m, .77 m, and .77 m. A Bonneville cross-flow heat exchanger is located within each plenum. As the air exits the heat exchanger, and the second plenum, the air passes into a 0.22 m outer diameter pipe, which contains the ASME Standard orifice plate employed to measure the air mass flow rate. This pipe then connects to the 0.635 m by 0.635 m side of a plenum. Upon entering this plenum, the air first encounters a flow baffle used to distribute the flow, a honeycomb, and other flow straightening devices. These are followed by the impingement plenum (or upper plenum, located below the honeycomb and flow straightening devices, as shown in Fig. 2) whose top dimensions are 0.635 m and 0.635 m, and whose height is 0.40 m.

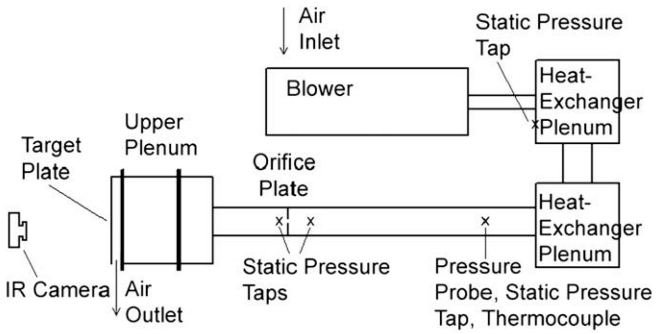

Fig. 1. Impingement flow facility.

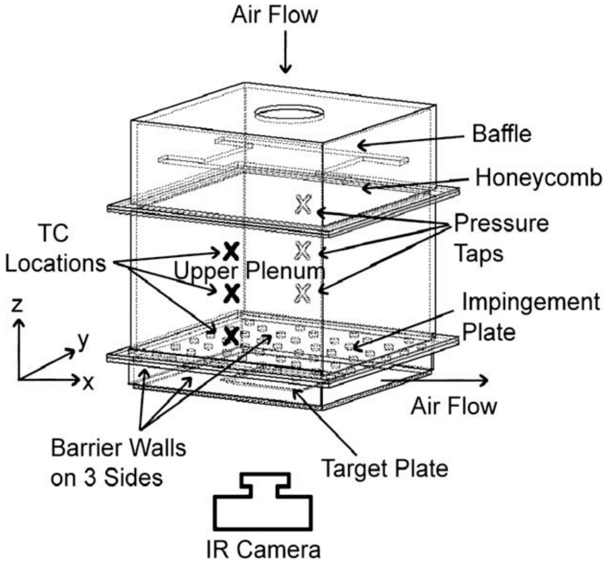

Fig. 2. Impingement flow facility test section, including impingement plenum, and impingement channel.

Individual plates with holes used to produce the impingement jets are located at the bottom of this plenum, as shown in Fig. 2. The plenum is thus designed so that different impingement plates can be installed at this location. Fig. 3 shows that each impingement plate is arranged with 10 rows of holes in the streamwise direction, arranged so that holes in adjacent rows are staggered with respect to each other. With this arrangement, either 9 or 10 holes are located in each streamwise row. The spacings between holes in the streamwise direction X are then either $8D$ or $12D$, and the spanwise spacings between holes in a given streamwise row Y are also either $8D$ or $12D$. The thickness of each impingement plate is $1D$. The spacing between the hole exit planes and the target plate is denoted Z and is equal to $3D$. Note that the coordinate systems employed are also shown in Fig. 3. The impingement cooling flow which issues from these holes is contained within the channel formed by the impingement jet plate and the target surface, and is constrained to exit in a single direction, which here, is denoted as the x-direction. This channel is called the lower

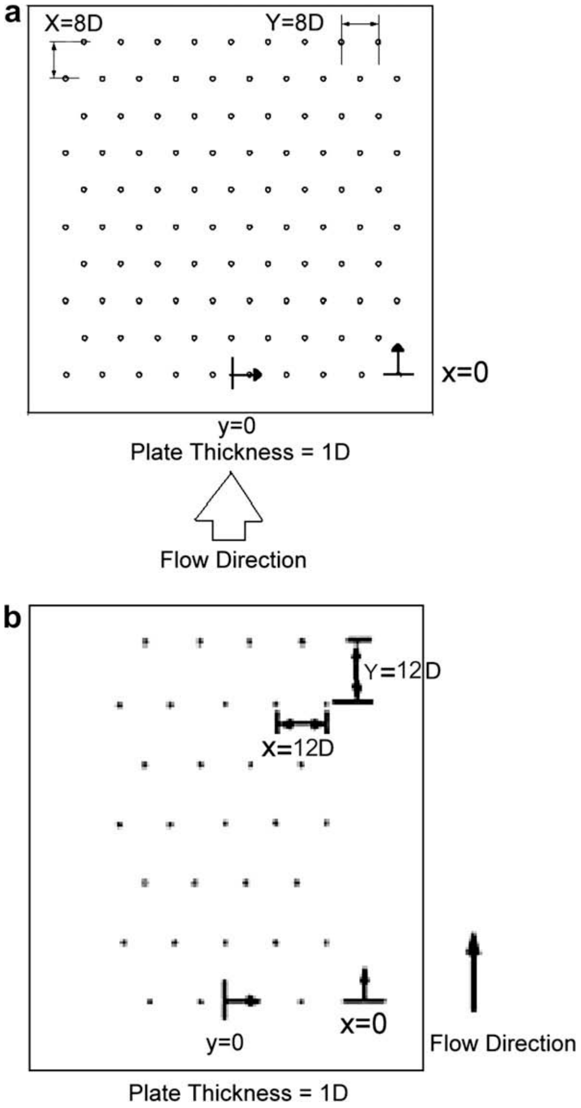

Fig. 3. Impingement test plate configurations: (a) $X/D = Y/D = 8$ and (b) $X/D = Y/D = 12$.

plenum. In the present study, the hole diameter size, D, blower, mass flow rate, and pressure level are employed so that the Mach number ranges from 0.1 to 0.6 and the Reynolds number is between 8200 and 30,500.

2.2. Target plate test surfaces for measurements of surface Nusselt numbers

The polystyrene target plate is 1.58 mm thick, and is mounted on the bottom surface of the plenum using grey cloth tape with PVC cement, a solvent containing methyl-ethyl-ketone, tetrahydrofuran, and acetone to seal the edges so that no leaks are present along the flow passage. A mounting frame is also employed to hold the solid polystyrene target plate in place, and to keep it smooth (without bending or wrinkles), and normal to the impingement jets, as testing is underway. Ten calibrated, copper–constantan thermocouples are placed at different streamwise and spanwise locations within the polystyrene target plate so that each senses a different temperature as data are acquired. Each one of these thermocouples is mounted approximately 0.016 cm just below the surface adjacent to the air containing the impingement fluid. These provide measurements of local surface temperatures, after correction for thermal contact resistance and temperature drop through the 0.016 cm thickness of polystyrene. Thermocouple lead wires are placed in grooves along the polystyrene, and bonded into place with epoxy having approximately the same thermal conductivity as polystyrene, to minimize thermal disturbances resulting from their presence. Each one of these thermocouple wires is then located between the thermofoil heater and the polystyrene portion of the target plate.

Spatially-resolved distributions of surface heat transfer coefficients and Nusselt numbers are measured on the polystyrene target plates with heaters and thermocouples attached. The custom-made HK5184R26 thermofoil heaters employed are manufactured by Minco Products Inc., and have a temperature rating of 100 °C. The etched-foil heating element within this device is encased between two layers of DuPont Kapton polyimide film. This heater is located adjacent to the air stream with the impinging air jets to provide a constant surface heat flux boundary condition adjacent to the impingement air stream. Its thermal conductivity is approximately 0.2 W/m K at 20 °C. Polystyrene is chosen for the target plate because of its strength, and because it does not deform in shape at temperatures as high as 80 °C. It is also suitable because of its relatively low thermal conductivity (0.09 W/m K at 20 °C), which results in minimal streamwise and spanwise conduction along the test surface. The back side of this polystyrene plate is viewed by the infrared camera as spatially-resolved measurements of surface temperature are obtained. Each polystyrene target plate is 1.27 mm thick and each heater is approximately 0.3 mm thick, giving a total target plate thickness of 1.57 mm. Because of the wear and degradation which results from exposure to different temperature levels as tests are conducted, these target plates are replaced with all new components after each three or four individual test sequences.

2.3. Local impingement air pressure and temperature measurements

As shown in Fig. 2, three wall static pressure taps are located on the surface of the upper plenum. Eight wall pressure taps are also located on the surface of the lower plenum for measurement of local static pressures. As tests are conducted, Validyne Model DP15-46 pressure transducers (with diaphragms rated at 13.8 or 34.5 kPa) driven by DP10D Carrier Demodulators are used to sense pressures from these static pressure tappings. Local airflow recovery temperatures are measured using two calibrated copper-constantan thermocouples located in the central part of the lower plenum, and three calibrated copper-constantan thermocouples located in the central part of the upper plenum. In each case, readings from either multiple thermocouples or multiple pressure taps are used to obtain average values of measured quantities for a given plenum. Voltages from the carrier demodulators and all thermocouples employed in the study are read sequentially using Hewlett-Packard HP44222T and HP44222A relay multiplexer card assemblies, installed in a Hewlett-Packard HP3497A low-speed Data Acquisition/ Control Unit. This system provides thermocouple compensation electronically such that voltages for type T copper-constantan thermocouples are given relative to 0 °C. The voltage outputs from this unit are acquired by the Dell Precision 530 PC workstation through its USB port, using LABVIEW 7.0 software and a GPIB-USB-B adaptor made by National Instruments.

Because the overall volume and cross-sectional area of the upper plenum are large compared to the area of the impingement holes, the velocity and Mach number of the air in this plenum are both near zero. As a result, the static pressure measured at the wall static pressure taps is the same as the stagnation pressure, and is denoted P_{oj}, the impingement air stagnation pressure. The measured air recovery temperature in the upper plenum is then the same as the upper plenum static temperature and upper plenum stagnation temperature. This resulting value is denoted T_{oj}, the impingement stagnation temperature. After measurement of the impingement air mass flow rate at the pipe orifice plate, the impingement air mass flux is determined using $\rho_a \mu_a = \dot{m}/A$.

An iterative procedure is then used to determine the impingement static temperature T_j, and the impingement flow Mach number Ma. The first step in this procedure is estimation of the value of T_j. The local recovery temperature, which is measured in the lower plenum, is used for this estimation. The impingement static density, and spatially-averaged impingement jet velocity are then determined using $\rho_a = P_a/RT_j$, and $u_a = \dot{m}/\rho_a A$, respectively. Because the impingement flow vents to the laboratory, the local atmospheric pressure is used for P_a. Measurements of lower plenum static pressures using wall pressure taps confirm this approach. Next, the impingement air sonic velocity and Mach number are given by $c_a = (kRT_j)^{1/2}$ and $Ma = u_a/c_a$, respectively. Iterations using these analysis steps are then continued until the impingement static temperature and impingement Mach number are consistent with the isentropic equation given by

$$T_j = T_{oj}/[1 + Ma^2(k-1)/2] \tag{1}$$

With impingement static temperature T_j, impingement flow Mach number Ma, and other parameters known, the impingement Reynolds number is subsequently given by an equation of the form

$$Re_j = \rho_a \mu_a D/\mu \tag{2}$$

A Kiel-type stagnation pressure probe is used to measure the total pressure in the pipe at a position which is located upstream of the orifice plate employed to measure mass flow rate. A wall pressure tap located on the surface of the pipe, and a calibrated copper-constantan thermocouple positioned within the air stream are used to sense static pressure and flow recovery temperature, respectively, at the same streamwise location. Pressures and temperatures measured using the thermocouple, probe, and tap are sensed and processed using the same types of instrumentation mentioned earlier. The velocities deduced from this arrangement are used to provide a cross-check on the velocities deduced from mass flow rates, which are measured using the ASME standard orifice plate.

2.4. Local Nusselt number measurement

The power to the thermofoil heater, mounted on the target plate, is controlled and regulated using a variac power supply. Energy balances, and analysis to determine temperature values on the two surfaces of the target plate, then allow determination of the magnitude of the total convective power (due to impingement cooling) for a particular test. To determine the surface heat flux (used to calculate heat transfer coefficients and local Nusselt numbers), the total convective power level, provided by the particular thermofoil heater employed, is divided by the single surface area of this heater, denoted A_{ht}.

One step in this procedure utilizes a one-dimensional conduction analysis, which is applied between the surface *within* the target plate where the thermocouples are located (between the heater and the polystyrene target plate), and the ambient air environment behind the target plate. This is used to determine T_b, the local temperature on the back surface of the polystyrene target plate, adjacent to the surrounding ambient air environment. Also required for this analysis is T_{tc}, the local temperature within the target plate between the heater and the polystyrene plate, which is determined from thermocouple measurements. With these temperatures known, the radiation heat flux and the convection heat flux from the back side of the target plate, q_{rb} and q_{cb}, respectively, are determined together using an equation of the form

$$q_{rb} + q_{cb} = h_{loss}(T_b - T_{ambient}) \tag{3}$$

where h_{loss} is assumed to be equal to 15 W/m^2 K [21]. The radiation heat flux q_{rf} on the front (or impingement side) of the target plate is determined using

$$q_{rf} = \sigma(1/\varepsilon_{inf} - 1/\varepsilon_f - 1)^{-1}(T_W^4 - T_{ambient}^4) \tag{4}$$

With this approach, the radiation heat flux is determined for an arrangement with multi-reflection between two infinite plates where each has a uniform temperature. ε_f and ε_{inf} are assumed to be equal to 0.9 for all conditions investigated. This approximate approach works well since $q_{rf}A_{ht}$ is generally only 3–6 percent of Q, the total amount of power provided to the thermofoil heater. Note that T_W, the local target surface temperature on the surface of the heater adjacent impingement air, must be known to determine q_{rf}. Because of the inter-dependence of T_W, q_{rf}, and q_{cf} (the convection heat flux from the front side or impingement side of the target plate), an iterative procedure is required to determine these quantities. The next part of this procedure uses a one-dimensional conduction model for the heater, which includes source generation of thermal energy, to provide a relation between T_W, T_{tc}, and q_{cf}. Also included in the analysis is thermal contact resistance between the internal thermocouples and the adjacent heater.

The convection heat flux from the front side (or impingement side) of the target plate is then given by

$$q_{cf} = Q/A_{ht} - q_{rf} - q_{rb} - q_{cb} \tag{5}$$

The local Nusselt number is then given as

$$Nu = q_{cf}D/((T_W - T_{oj})\alpha) \tag{6}$$

As impingement heat transfer measurements are made, spatially-resolved distributions of the target test surface temperature T_W are determined using infrared imaging in conjunction with thermocouples, energy balances, digital image processing, and *in situ* calibration procedures. These are then used to determine spatially-resolved surface Nusselt numbers. To accomplish this, the infrared radiation emitted by the heated interior surface of the channel is captured using a FLIR Systems Inc. ThermoVision® A20M Compact Temerature Measurement IR Camera (S/N 22700776), which operates at infrared wavelengths from 7.5 to 13.0 μm. Temperatures, measured using the calibrated, copper-constantan thermocouples distributed along the test surface adjacent to the flow, are used to perform the *in situ* calibrations simultaneously as the radiation contours from surface temperature variations are recorded.

This is accomplished as the camera views the test surface from behind, as shown in Fig. 2. In general, all ten thermocouple junction locations are present in the infrared field viewed by the camera. The exact spatial locations and pixel locations of these thermocouple junctions and the coordinates of the field of view are known from calibration maps obtained prior to measurements. During this procedure, the camera is focused, and rigidly mounted and oriented relative to the test surface in the same way as when radiation contours are recorded. Voltages from the thermocouples are acquired using the apparatus mentioned earlier. With these data, gray scale values at pixel locations within digital images from the infrared imaging camera are readily converted to local Nusselt number values. Because such calibration data depend strongly on camera adjustment, the same brightness, contrast, and aperture camera settings are used to obtain the experimental data. The *in situ* calibration approach rigorously and accurately accounts for these variations.

Images from the infrared camera are recorded as 8-bit gray scale directly into the memory of a Dell Dimension XPS T800r PC computer using a Scion Image Corporation Frame grabber video card, and Scion image v.1.9.2 software. One set of 15–20 frames is recorded at a rate of about one frame per second. All of the resulting images are then ensemble averaged to obtain the final gray scale data image. This final data set is then imported into Matlab software to convert each of 256 possible gray scale values to local Nusselt number at each pixel location using calibration data. Each individual image covers a 256 pixel by 256 pixel area.

2.5. Crossflow mass velocity-to-jet mass velocity ratio and discharge coefficient

The crossflow-to-jet mass velocity ratio G_c/G_j is given by

$$\frac{G_c}{G_j} = \frac{\text{crossflow mass velocity}}{\text{jet mass velocity}} = \frac{\rho u_{\text{crossflow}}}{\rho u_{\text{jet}}} \tag{7}$$

Discharge coefficients are determined using

$$C_D = \rho_a \mu_a / \rho_i \mu_i \tag{8}$$

The first step in determining the ideal impingement mass flux $\rho_i \mu_i$ is obtaining an ideal impingement Mach number *Mi* using

$$P_{oj}/P_a = [1 + Mi^2(k-1)/2]^{k/k-1} \tag{9}$$

Next, impingement ideal static temperature T_i is determined using T_{oj}, the ideal Mach number *Mi*, and the appropriate ideal gas isentropic relationship. Impingement ideal static density is given by $\rho_i = P_a/RT_i$, and impingement ideal velocity is given by $\mu_i = Mi(kRT_i)^{1/2}$. Note that, in most cases, discharge coefficients are determined which are based on P_a, the spatially-averaged static pressure at the exits of the impingement holes. P_a is measured by using a OMEGA HHP-102F pressure sensor.

2.6. Experimental uncertainty estimates

Uncertainty estimates are based on 95% confidence levels and are determined using methods described by Kline and McClintock [28] and Moffat [29]. Uncertainty of temperatures measured with thermocouples is ±0.15 °C. Spatial and temperature resolutions achieved with infrared imaging are about 0.1–0.2 mm, and 0.4 °C, respectively. This magnitude of temperature resolution is due to uncertainty in determining the exact locations of thermocouples with respect to pixel values used for the *in situ* calibrations. Local Nusselt number uncertainty is then about ±4.8%. Note that uncertainties of local Nusselt numbers include the effects of very small amounts of streamwise and spanwise conduction along the test surfaces employed. Reynolds number uncertainty is about ±2.0% for Re_j values of 17,000–20,000.

Table 1
Impingement test plate configurations

Hole diameter (mm)	Plate thickness (mm)	Hole spacing, *X*, *Y*
3.5	3.5	28
3.5	3.5	42
4.5	4.5	36
4.5	4.5	54
8	8	64
8	8	96
15	15	120
15	15	180

Table 2
Experimental conditions

Re_j	*Ma*	*D* (mm)	*X*/*D*,*Y*/*D*
8200	0.10	4.5	8
17,300	0.20	4.5	8
30,000	0.11	15	8
30,500	0.20	8	8
30,000	0.35	4.5	8
31,000	0.45	3.5	8
8400	0.10	4.5	12
17,200	0.20	4.5	12
30,000	0.11	15	12
30,500	0.20	8	12
30,000	0.35	4.5	12
31,000	0.45	3.5	12

3. Experimental results and discussion

Table 1 gives the impingement test plate configurations. Table 2 gives the experimental conditions of the present investigation.

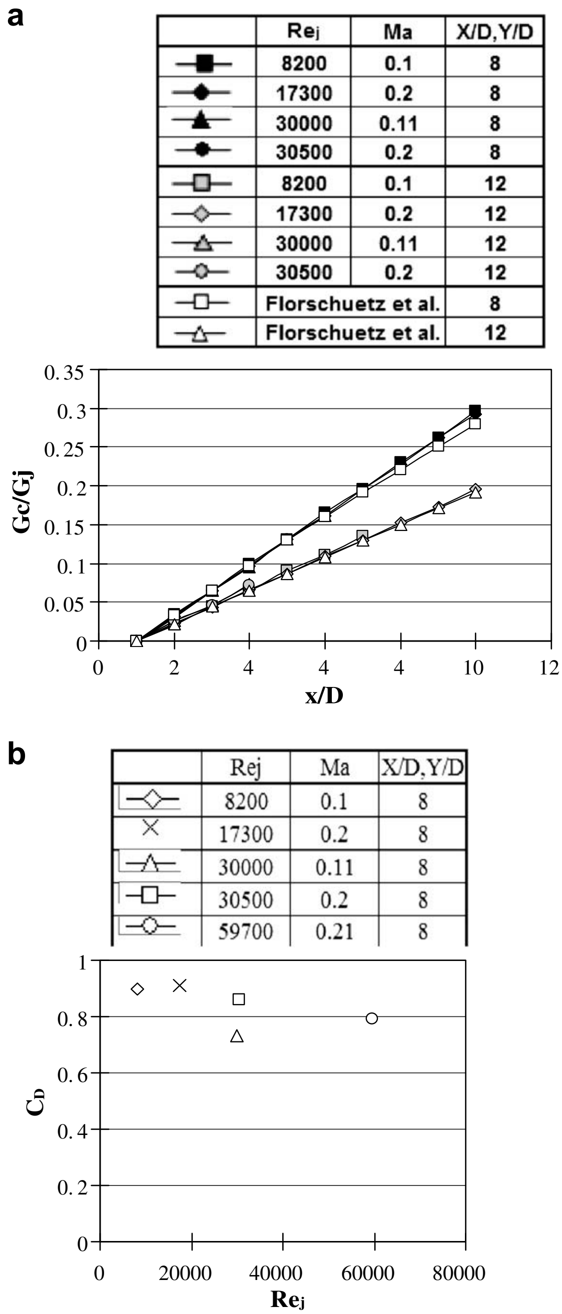

Fig. 4. (a) Crossflow-to-jet mass velocity ratio variations with *x*/*D* for hole spacings of 8*D* and 12*D* and (b) discharge coefficient variations with Re_j for a hole spacing of 8*D*.

3.1. Crossflow mass velocity-to-jet mass velocity ratio and discharge coefficients

Fig. 4a shows the ratio of crossflow mass velocity-to-jet mass velocity as it varies with x/D for hole spacings of 8D and 12D. This ratio is only as high as about 0.3 at the end of all rows of holes. Here, data from the present study show reasonably good agreement with the correlation of Florschuetz et al. [9]. Note that, G_c/G_j values are lower for 12D hole spacing than for 8D hole spacing when compared at a particular value of x/D. Discharge coefficients represent average values for all of the impingement holes on a particular test plate, and are presented in Fig. 4b. From this graph, it is apparent that discharge coefficients decrease slightly as the Reynolds number increases.

3.2. Spatially-resolved local Nusselt numbers

Fig. 5a–h show spatially-resolved surface Nusselt number distributions for 12D and 8D hole spacings for Re_j = 8200, 17,300, 30,000, and 30,500, and Ma = 0.1, 0.2, 0.11, and 0.2, respectively. Note that the Ma = 0.11 and Ma = 0.2 data are considered in order to establish the extent of Mach number dependence of local Nusselt number data, as the injection jet Reynolds number Re_j is maintained constant. The different views of the test surface are due to different infrared camera views of the target plate as different impingement plates with different Reynolds number and Mach number are employed. This is because the impingement plates which are employed are different sizes with different sizes of hole diameters. Note that, regardless of the Reynolds number and the Mach number, that the qualitative distributions of local Nusselt numbers produced by each impingement jet are similar, with good periodic repeatability in the spanwise direction for each streamwise row of impact location. Fig. 5a–d also show that local Nusselt number *peak values* for 12D hole spacing generally become smaller at successive x/D locations for each value of impingement jet Reynolds number and Mach number due to the detrimental effect spent air crossflow has on heat transfer. Fig. 5e–h show comparable results for 8D hole spacing. Here, local Nusselt number

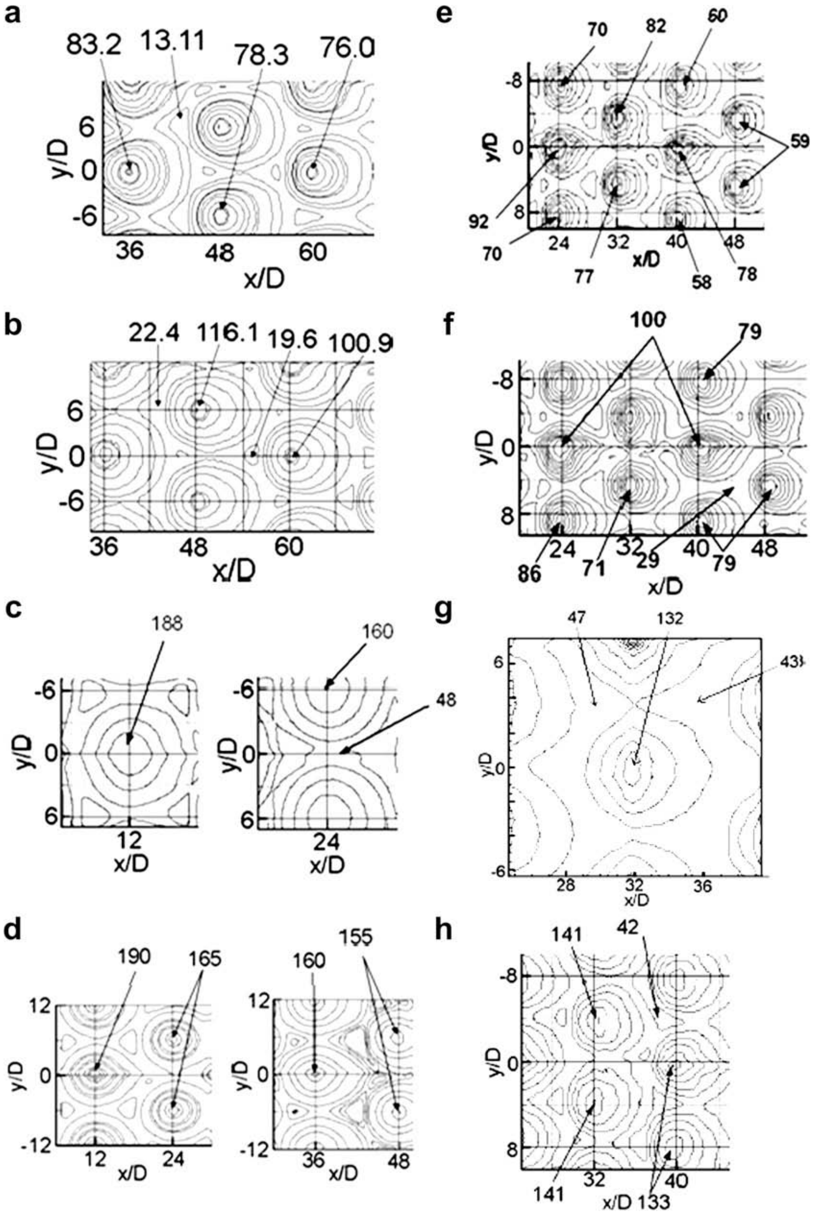

Fig. 5. Local Nusselt number variations: (a) Re_j = 8200, Ma = 0.1, $X = Y$ = 12D, (b) Re_j = 17,300, Ma = 0.2, $X = Y$ = 12D, (c) Re_j = 30,000, Ma = 0.11, $X = Y$ = 12D, (d) Re_j = 30,500, Ma = 0.2, $X = Y$ = 12D, (e) Re_j = 8200, Ma = 0.1, $X = Y$ = 8D, (f) Re_j = 17,300, Ma = 0.2, $X = Y$ = 8D, (g) Re_j = 30,000, Ma = 0.11, $X = Y$ = 8D and (h) Re_j = 30,500, Ma = 0.2, $X = Y$ = 8D.

decreases with x/D for 8D hole spacing are generally more pronounced at most all x/D locations (compared to the 12D hole spacing data). This is a result of the cumulative effects of the interactions between adjacent jets and the resulting cross-flows for an arrangement where the jets are more closely spaced together. Note that the experimental conditions for the results in Fig. 5a and e, Fig. 5b and f, Fig. 5c and g, Fig. 5d and h, respectively, are similar. For all four comparisons, quantitative magnitudes of local peak Nusselt numbers are generally similar.

These variations are further illustrated by local Nusselt number data presented in Fig. 6. Fig. 6a shows local Nusselt number variations with y/D for $x/D = 24$ and 48. Here, local peak values are located near $y/D = -6$ and $y/D = 6$ underneath impinging jet impact locations. Fig. 6b presents local Nusselt number data as it varies with x/D for $y/D = 0$. Here, local maximum values are apparent, which are spaced approximately 24D apart, which are due to the impact of impingement jets from each different streamwise row of holes.

Fig. 7a and 7b present local Nusselt number comparisons for hole spacings of 8D and 12D as dependent upon y/D for particular values of x/D, and as dependent upon x/D for particular values of y/D, respectively. In general, lower local values are present between jet impact locations for 12D hole spacing than for 8D hole spacing in Fig. 7a and 7b, when compared at the same Re_j, and Ma. Peak local Nusselt numbers for 8D and 12D hole spacings in Fig. 7a are about the same when compared at the same Re_j, and Ma. Referring to the $X/D = Y/D = 12$ data in Fig. 7a, local Nusselt numbers at each y/D location increase continually as the impingement jet Reynolds number Re_j increases. These data also appear to be approximately independent of jet Mach number, which is illustrated by the agreement between the $Re_j = 30{,}000$, $Ma = 0.11$ data set, and the $Re_j = 30{,}500$, $Ma = 0.2$ data set.

In regard to the physical interactions, the variations due to different impingement jet spacings are, in part, because each jet produced using the larger spacing of $X/D = Y/D = 12$ approximates the behavior of an individual jet. When $X/D = Y/D = 8$, the influences of surrounding jets, including the cumulative induced cross-flows, reduce the effectiveness of each individual jet. The present data provide evidence that these detrimental effects for the smaller hole spacing become more significant as either Mach number or

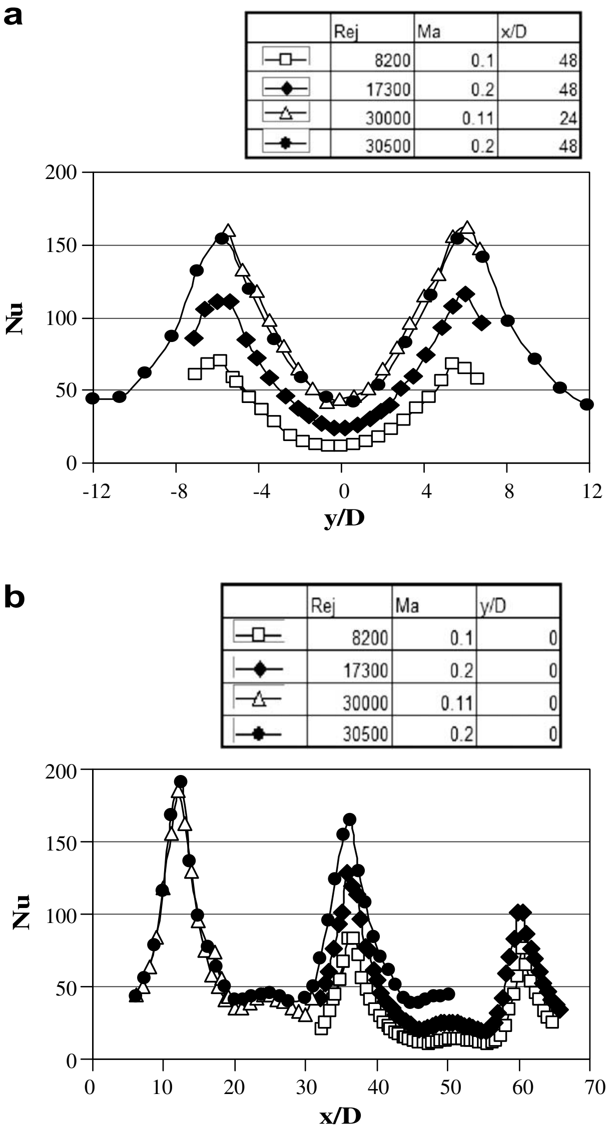

Fig. 6. Local Nusselt number variations for a hole spacing of 12D: (a) variations with y/D for $x/D = 24$ and 48 and (b) variations with x/D for $y/D = 0$.

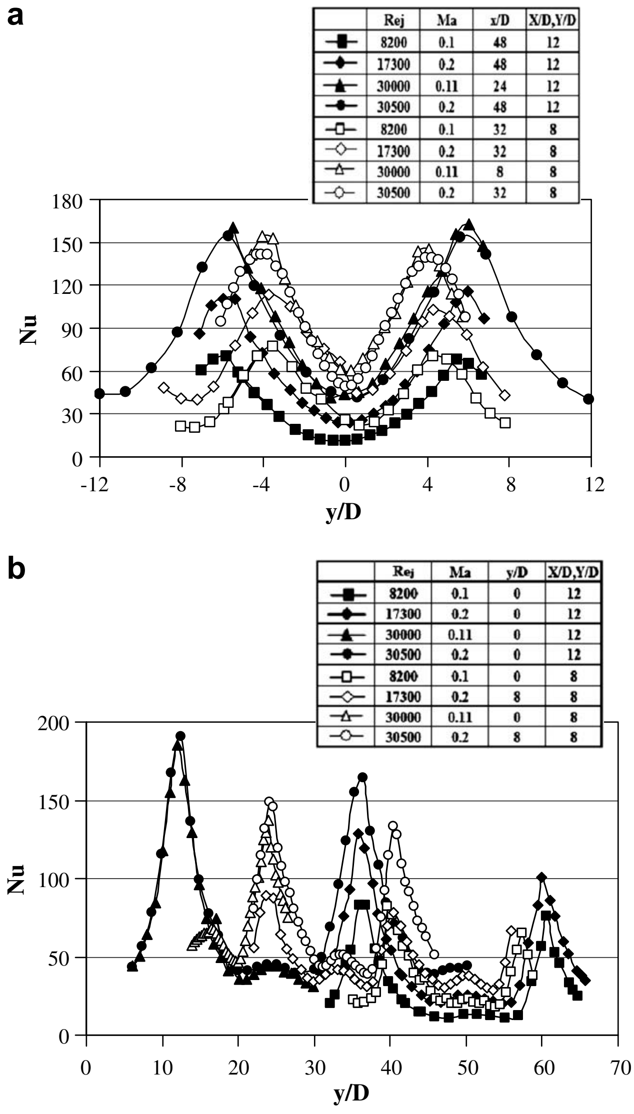

Fig. 7. Comparisons of results for 8D and 12D hole spacings: (a) local Nusselt numbers as they vary with y/D at $x/D = 24$, 32, and 48 and (b) local Nusselt numbers as they vary with x/D at $y/D = 0$, and 8.

Reynolds number increases, even when the average impingement jet Mach number is only as high as 0.2. Also of importance are the vortices which form around the impinging jets, and then interact with each other after they impact on the target surface [12]. These influences result in almost no change between the results presented in Fig. 5c and 5d for $X/D = Y/D = 12$. The same is true for the results presented in Fig. 5g and 5h for $X/D = Y/D = 8$. One important result of this influence is accumulation of cross-flows from sequential rows of jets, which is especially apparent for the 8D jet spacing and gives a general trend of decreasing Nusselt numbers with x/D. These variations are also evident in Fig. 7a and 7b, which show that the changes are generally most apparent in local values (i.e. with smaller periodic variation with x/D or y/D), than values which are line-averaged or area-averaged.

3.3. Line-averaged Nusselt numbers

Fig. 8 presents Nusselt numbers which are line-averaged over y/D from −6.0 and +6.0 for a hole spacing of 12D. Here, the 12D spacing data sets for $Re_j = 30{,}000$, $Ma = 0.11$, and $Re_{jj} = 30{,}500$, $Ma = 0.2$ are similar. As Re_j then decreases, $\bar{N}u$ data then also decrease at each x/D value. Overall, this behavior indicates strong dependence on Reynolds number Re_j and negligible dependence on Mach number for $Ma \leqslant 0.2$ for 12D jet spacing.

Comparisons of line-averaged Nusselt number data for hole spacings of 8D and 12D are shown in Fig. 9. Notice that periodic line-averaged Nusselt numbers generally decrease at the successive x/D locations for $X/D = 8$, whereas periodic $X/D = 12$ data are approximately invariant with x/D. With larger hole spacing, cumulative crossflow mass velocities are smaller, and the behavior of each impingement jet approximates that of a single jet, as mentioned. Like the data in the previous figure, Fig. 9 shows that the 8D jet spacing data also show strong dependence on Reynolds number Re_j. Fig. 9 shows $\bar{N}u$ values with almost no dependence on Mach number, provided the jet Mach number Ma is less than or equal to 0.2. This is consistent with the data in Fig. 7 and provides additional evidence that the compressible interactions between jets which are present for $Re_j = 30{,}500$ and $Ma = 0.2$ mostly affect local Nu distributions, rather than spatially-averaged Nusselt number data. When compared at the same Re_j and Ma values, peak $\bar{N}u$ values in Fig. 9 for 8D and 12D hole spacings are similar in magnitude, whereas $\bar{N}u$ values at locations midway between $\bar{N}u$ peaks are generally lower for 12D hole spacing than for 8D hole spacing. This is due to the manner in which fluid contained in the jets interacts with fluid from adjacent jets, as it advects away from individual stagnation points.

These interactions are tied to the unteady vortex structures and vortex rings which initially form around the periphery parts of the impingement jets. According to Fox et al. [12], it is the competition between these vortex rings and the associated secondary vortices induced by them which determine the local stagnation temperature and static temperature distributions on the impingement target plate. The resulting total temperature alterations from these vortices are then also responsible for enhancing the surface heat transfer and the surface Nusselt number distributions. Depending

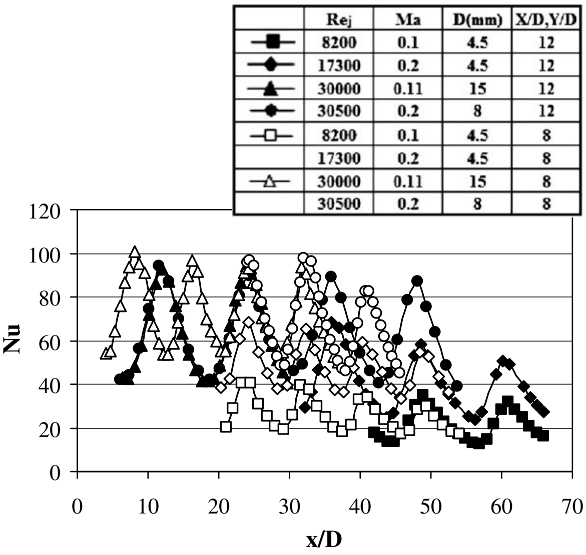

Fig. 9. Line-averaged Nusselt numbers for comparison of 8D and 12D hole spacings.

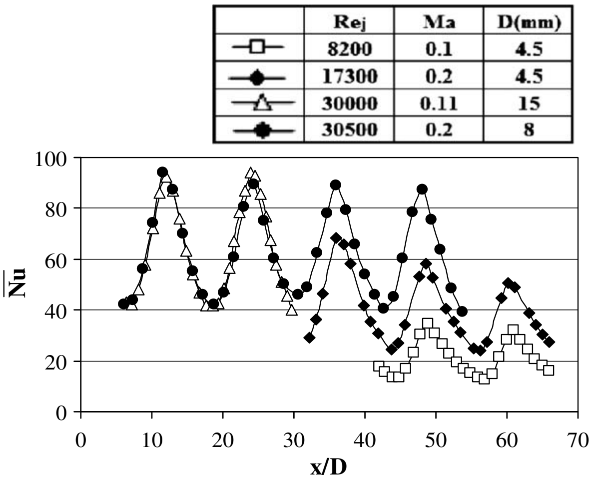

Fig. 8. Line-averaged Nusselt numbers as dependent upon x/D for 12D hole spacing.

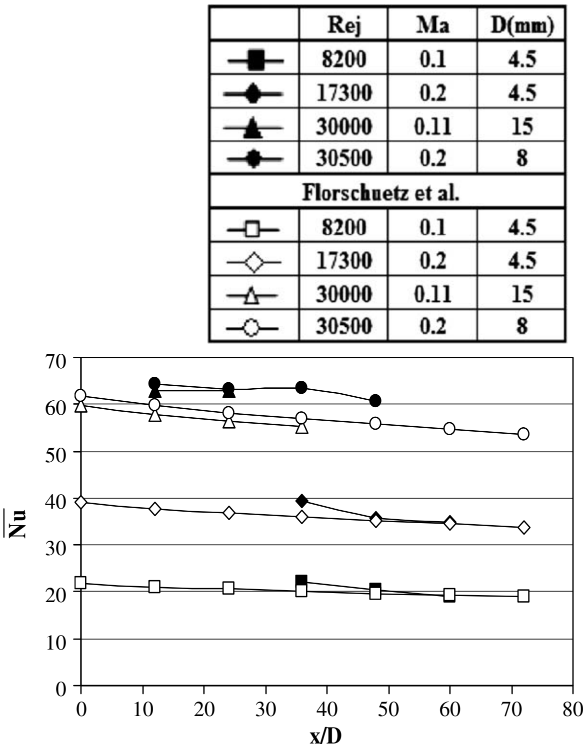

Fig. 10. Spatially-averaged Nusselt numbers as dependent upon x/D for 12D hole spacing.

upon the interactions between the primary and secondary vortex rings after they impact and advect along the target plate, different amounts and distributions of surface heating and/or cooling can be produced [12]. Compressibility, even in a mild form, alters these complex vortex interactions. Complications and complexity also result as the vortex rings and the associated secondary vortices from different impingement jets intermingle and interact with each other in a myriad of possible forms and combinations.

3.4. Spatially-averaged Nusselt numbers

Spatially-averaged Nusselt numbers for 12*D* hole spacing are compared to values from Florschuetz et al. [9] in Fig. 10. These data are given for Reynolds numbers of 8200, 17,300, 30,000, and 30,500, and Mach numbers of 0.1, 0.2, 0.11, and 0.2, respectively. Here, data from the present study for $Re_j = 8200$, $Ma = 0.1$, and $Re_j = 17{,}300$, $Ma = 0.2$ are about equal to correlation predicted values [9]. Data from the present study for $Re_j = 30{,}000$, $Ma = 0.11$, and $Re_j = 30{,}500$, $Ma = 0.2$ for 12*D* hole spacing are outside the range of applicability of the Florschuetz et al. [9] correlation, which does not consider geometries with hole spacing greater than 8*D* for a staggered array. It is therefore not surprising that the present data are slightly higher than correlation predicted values. Spatially-averaged Nusselt numbers for jet hole spacings of 12*D* and 8*D* are compared in Fig. 11. Here, spatially-averaged Nusselt numbers for 8*D* jet hole spacing are generally higher than values for 12*D* jet hole spacing when compared at the same Re_j, Ma, and x/D. The 12*D* jet hole spacing data also show less variation with x/D, which is consistent with data presented earlier.

	Rej	Ma	D(mm)	X/D,Y/D
■	8200	0.1	4.5	12
◆	17300	0.2	4.5	12
▲	30000	0.11	15	12
●	30500	0.2	8	12
□	8200	0.1	4.5	8
	17300	0.2	4.5	8
△	30000	0.11	15	8
	30500	0.2	8	8

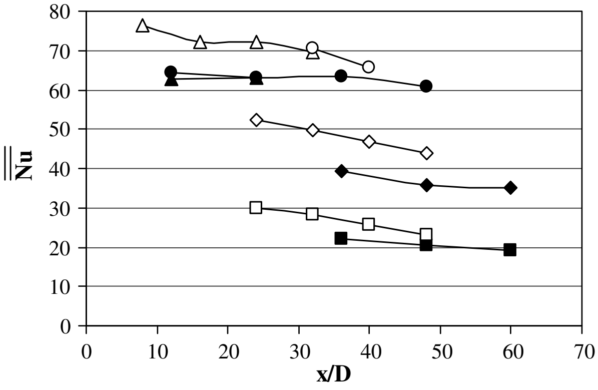

Fig. 11. Spatially-averaged Nusselt numbers for comparison of 8*D* and 12*D* hole spacings.

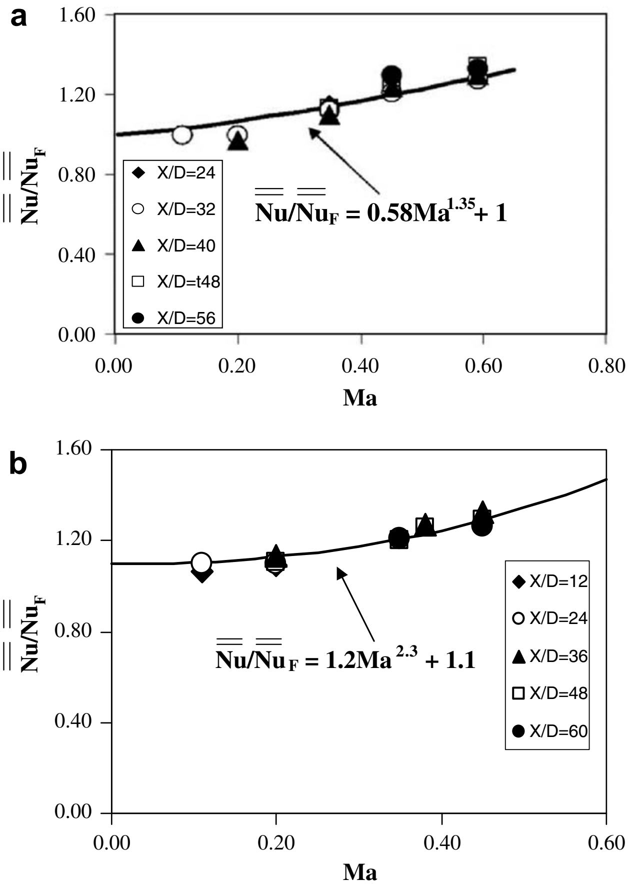

Fig. 12. Nusselt number correlation with Mach number: (a) hole spacing $X/D = 8$, $Re_j = 30{,}000$ and Ma values of 0.11, 0.20, 0.35, 0.45, and 0.60 and (b) hole spacing $X/D = 12$, $Re_j = 30{,}000$ and Ma values of 0.11, 0.20, 0.35, 0.37 and 0.45.

3.5. Compressible flow effects

Most existing correlations for arrays of impinging jets generally do not include compressible flow effects. To partially resolve this deficiency, spatially-averaged Nusselt numbers are compared to the correlation of Florscheutz et al. [9] for $Re_j = 30{,}000$ and $Ma = 0.11$, 0.20, 0.35, 0.45, and 0.60. Park et al. [30] give a correlation based on the Florscheutz correlation which accounts for Mach number effects at this Reynolds number $Re_j = 30{,}000$, for $0.1 \leqslant Ma \leqslant 0.6$, $X/D = 8$, $Y/D = 8$, $Z/D = 3$ and $24 \leqslant x/D \leqslant 56$. This correlation equation is given by [30]

$$\frac{\overline{\overline{Nu}}}{\overline{\overline{Nu}}_F} = 1.0 + 0.58Ma^{1.35} \tag{10}$$

and is shown in Fig. 12a. The present study provides data also for $Re_j = 30{,}000$ for hole spacing of $X/D = Y/D = 12$. The resulting new correlation is then given by

$$\frac{\overline{\overline{Nu}}}{\overline{\overline{Nu}}_F} = 1.1 + 1.2Ma^{2.3} \tag{11}$$

Fig. 12b then shows that Eq. (11) is valid for $Re_j = 30{,}000$, $0.1 \leqslant Ma \leqslant 0.6$, $X/D = 12$, $Y/D = 12$, $Z/D = 3$ and $12 \leqslant x/D \leqslant 60$.

4. Summary and conclusions

Incompressible and compressible jet array impingement data are provided as the jet hole spacing is varied for Reynolds number values of 8200, 17,300, 30,000, and 30,500 and Mach number values as high as 0.60. The spacings between holes in the streamwise direction *X* are then either 8*D* or 12*D*, and the spanwise spacings between holes in a given streamwise row *Y* are also either 8*D* or 12*D*. The thickness of each impingement plate is 1*D*, and the spacing between the hole exit planes and the target plate is denoted *Z* and is equal to 3*D*. These data are given for an array of impinging jets in the form of ratios of crossflow mass velocity to jet mass velocity, discharge coefficients, spatially-resolved local surface Nusselt numbers, line-averaged Nusselt numbers, and spatially-averaged Nusselt numbers.

For both jet spacings and $X/D = Y/D = 12$ and $X/D = Y/D = 8$, local, line-averaged, and area-averaged data show strong Reynolds number dependence, but almost no dependence on Mach number, provided the impingement jet Mach number is less than about 0.2. Each jet produced using $X/D = Y/D = 12$ approximates the behavior of an individual jet, whereas the influences of surrounding jets, including the cumulative induced cross-flows and interactions of jet-induced vortex structures, alter the effectiveness of each individual jet when $X/D = Y/D = 8$. Spatially-averaged Nusselt numbers for $8D$ jet spacing are generally higher than values for $12D$ jet spacing when compared at the same streamwise location. The $12D$ jet spacing data also show less variation with x/D. Comparisons of periodic line-averaged Nusselt number data show that values generally decrease at successive x/D locations for $X/D = Y/D = 8$, whereas $X/D = Y/D = 12$ data are approximately invariant with x/D. Regardless of the Reynolds number and the Mach number, the qualitative local Nusselt number distributions produced by different impingement jets are similar, with good periodic repeatability in the spanwise direction for each row of streamwise impact location. Crossflow mass velocity-to-jet mass velocity ratio data are lower for $12D$ jet spacing than for $8D$ jet spacing when compared at a particular value of x/D, with reasonably good agreement with the correlation of Florschuetz et al. [9].

Both the data reported by Park et al. [30] and the data of the present study show strong dependence on Mach number, for Mach numbers greater than 0.2, as Reynolds number is held constant. Increasing the Mach number improves heat transfer for the X/D, $Y/D = 8$ geometry. The performance of the cooling jet array for the X/D, $Y/D = 12$ geometry also increases as Mach number increases. This is partially a result of the tendency of jets in sparse impingement arrays to behave more like independent jets [13].

Acknowledgement

The research presented in this paper was sponsored by Solar Turbines Inc., located in San Diego, California.

References

[1] H. Martin, Heat and mass transfer between impinging gas jets and solid surfaces, Advances in Heat Transfer, vol. 13, Academic Press, New York, 1977. pp. 1–60.
[2] A. Schulz, Combustor liner cooling technology in scope of reduced pollutant formation and rising thermal efficiencies, heat transfer in gas turbine systems, Ann. NY Acad. Sci. 934 (2001) 135–146.
[3] D.M. Kercher, W. Tabakoff, Heat transfer by a square array of round air jets impinging perpendicular to a flat surface including the effect of spent air, ASME Trans.–J. Eng. Power 92 (1970) 73–82.
[4] D.E. Metzger, T. Yamashita, C. Jenkins, Impingement cooling of concave surfaces with lines of circular air jets, ASME Trans.–J. Eng. Power 91 (1971) 149–158.
[5] R. Chupp, H. Helms, P. McFadden, T. Brown, Evaluation of internal heat-transfer coefficients for impingement cooled turbine airfoils, AIAA–J. Aircr. 6 (3) (1969) 203–208.
[6] D.E. Metzger, R. Korstad, Effects of crossflow on impingement heat transfer, ASME Trans.–J. Eng. Power 94 (1972) 35–41.
[7] J.L. Chance, Experimental investigation of air impingement heat transfer under an array of round jets, TAPPI 57 (6) (1974) 108–112.
[8] D.E. Metzger, L.W. Florschuetz, D.I. Takeuchi, R.D. Behee, R.A. Berry, Heat transfer characteristics for inline and staggered arrays of circular jets with crossflow of spent air, ASME Trans.–J. Heat Transfer 101 (1979) 526–531.
[9] L.W. Florschuetz, C.R. Truman, D.E. Metzger, Streamwise flow and heat transfer distributions for jet array impingement with crossflow, ASME Trans.–J. Heat Transfer 103 (1981) 337–342.
[10] N.T. Obot, T.A. Trabold, Impingement heat transfer within arrays of circular jets: Part 1–effects of minimum, intermediate, and complete crossflow for small and large spacings, ASME Trans.–J. Heat Transfer 109 (1987) 872–879.
[11] R. Bunker, D.E. Metzger, Local heat transfer in internally cooled turbine airfoil leading edge regions: Part 1 – impingement cooling without film extraction, ASME Trans.–J. Turbomach. 112 (1990) 451–458.
[12] M.D. Fox, M. Kurosaka, L. Hedges, K. Hirano, The influence of vortical structures on the thermal fields of jets, J. Fluid Mech. 255 (1993) 447–472.
[13] J.C. Bailey, R.S. Bunker, Local heat transfer and flow distributions for impinging jet arrays of dense and sparse extent, ASME Paper No. ASME GT-2002-30473, 2002.
[14] M.E. Taslim, Y. Pan, K. Bakhtari, Experimental racetrack shaped jet impingement on a roughened leading-edge wall with film holes, ASME Paper Number GT-2002-30477, 2002.
[15] X. Li, J.L. Gaddis, T. Wang, Mist/stream heat transfer with jet impingement onto a concave surface, ASME Paper No. GT-2002-30475, 2002.
[16] J.A. Parsons, J.C. Han, C.P. Lee, Rotation effect on jet-impingement heat transfer in smooth rectangular channels with four heated walls and radial crossflow, ASME Trans.–J. Turbomach. 120 (1996) 79–85.
[17] J.A. Parsons, J.C. Han, C.P. Lee, Rotation effect on jet-impingement heat transfer in smooth rectangular channels with four heated walls and coolant extraction, ASME Paper Number GT-2003-38905, 2003.
[18] J.A. Parsons, J.C. Han, Rotation effect on jet impingement heat transfer in smooth rectangular channels with coolant extraction, Int. J. Rotat. Mach. 7 (2001) 87–103.
[19] A.H. Epstein, J.L. Kerrebrock, J.J. Koo, U.Z. Preiser, Rotational effects on impingement cooling, Symposium on Transport Phenomena in Rotating Machinery, Honolulu, 1985.
[20] C. Mattern, D.K. Hennecke, Influence of rotation on impingement cooling, ASME Paper No. GT-1996-161, 1996.
[21] P. Brevet, C. Dejeu, E. Dorignac, M. Jolly, J.J. Vullierme, Heat transfer to a row of impinging jets in consideration of optimization, Int. J. Heat Mass Transfer 45 (2002) 4191–4200.
[22] P. Brevet, Dorignac, J.J. Vullierme, Mach number effect on jet impingement heat transfer, Heat Transfer in Gas Turbine Systems, Ann. NY Acad. Sci. 934 (2001) 409–416.
[23] A.I. Behbahani, R.J. Goldstein, Local heat transfer to staggered arrays of impinging circular air jets, J. Eng. Power 105 (1983) 354–360.
[24] J.-Y. San, M.-D. Lai, Optimum jet-to-jet spacing of heat transfer for staggered arrays of impinging air jets, Int. J. Heat Mass Transfer 44 (2001) 3997–4007.
[25] S.J. Downs, E.H. James, Jet impingement heat transfer-a literature survey, ASME Paper No. 87-HT-35, 1987.
[26] K. Jambunathan, E. Lai, M.A. Moss, B.L. Button, A review of heat transfer data for single circular jet impingement, Int. J. Heat Fluid Flow 13 (2) (1992) 106–115.
[27] R. Viskanta, Heat transfer to impinging isothermal gas and flame jets, Exp. Therm. Fluid Sci. 6 (1993) 111–134.
[28] S.J. Kline, F.A. McClintock, Describing uncertainties in single sample experiments, Mech. Eng. 75 (1953) 3–8.
[29] R.J. Moffat, Describing the uncertainties in experimental results, Exp. Therm. Fluid Sci. 1 (1) (1988) 3–17.
[30] J. Park, M. Goodro, P.M. Ligrani, M. Fox, H.-K. Moon, Separate effects of Mach number and Reynolds number on jet array impingement heat transfer, ASME Trans.–J. Turbomach. 129 (2007) 269–280.